IEEE Robotics and Automation Letters (RA-L) paper, presented at ICRA 2026, Vienna, Austria. Cite as RA-L paper.

Design and actuation of a multipole ring magnet for navigating endovascular magnetic instruments

Julian Raub[1], Lucio Pancaldi[1], Loic Von Deschwanden[1], Mahmut Selman Sakar[1]

***Abstract*—This paper presents the design and analysis of a compact magnetic field generator for robotic navigation of magnetic endovascular instruments in clinical settings. The system features eight symmetrically arranged permanent magnets in a ring configuration, maximizing magnetic field uniformity and aperture size for X-ray transmission while minimizing spatial footprint and magnet motion for uninterrupted fluoroscopy imaging. The rationale behind the design of the system is explained through analytical considerations of magnetic field distribution. In vitro demonstrations inside perfused biomimetic phantoms confirm the system's capability for 3D steering of flow-driven magnetic microcatheters, opening a path for pre-clinical testing.**

***Index Terms*—Magnetic navigation system, interventional radiology, magnetic microcatheters, medical robotics.**

I. Introduction

ENDOVASCULAR interventions based on the use of guidewires and catheters save patients suffering from cerebrovascular diseases such as aneurysms, arteriovenous malformations and stroke. Nevertheless, navigating distal brain vessels is still challenging due to complex and tortuous anatomy. Robotics and automation can improve the speed and safety of endovascular interventions, particularly with the use of magnetic actuation. Seminal work by Tillander in 1951 demonstrated the feasibility of navigating a catheter with a steel tip using external magnetic fields [1]. This work led to the development of a series of magnetic endovascular instruments in the following years, specifically for neurovascular interventions [2]–[5]. More recently, with the advancements in materials science and manufacturing, a new class of dexterous magnetic instruments have been introduced [6]–[12].

Robotic navigation systems that generate precisely controlled static magnetic fields are instrumental for the guidance of magnetic instruments [13], [14]. There are two basic clinical configurations of robotic navigation systems: a set of stationary electromagnets [8], [15], [16] and permanent magnet(s) manipulated around the patient [17]. This work aims to contribute to the development of the latter systems with the hope of harnessing the miniaturization capacity and cost-effectiveness of permanent magnets. An intuitive strategy followed by several research groups is to move one or two permanent magnets around the workspace using a robotic arm [7], [11], [18]. However, magnet mobility around the patient and the imaging system raises significant concerns regarding safety and imaging fidelity. Three dimensional (3D) rotation of a permanent magnet in place using a mechanical [19], [20] or electromechanical [12] mechanism addresses some of these concerns. Nevertheless, maintaining the position of the magnet at a distance limits the strength and distribution of the magnetic field within the workspace.

Catheterization procedures are performed in the hospital using a single (monoplane) or dual (bi-plane) C-arm fluoroscope system. The X-ray source of the fluoroscope casts a shadow of the vasculature and the medical instrument on the X-ray detector; therefore, the path of the X-ray radiation must be kept clear. We postulated that a robotic navigation system in the form of a flat panel with an aperture transparent to X-rays could be seamlessly placed between the source and the detector. Such a system would bring the magnetic field source close to the patient without compromising continuous fluoroscopic imaging. Moreover, a careful arrangement of an array of magnets within this panel would maximize the strength of magnetic fields generated in the workspace while preserving uniformity.

The steering of endovascular instruments involves bending of their magnetic tip. Bending is ideally achieved with the application of force-free magnetic torque, which is contingent upon the application of uniform magnetic fields. A Halbach array is a special arrangement of permanent magnets that focuses the magnetic field to be very strong on one side of the array while canceling it to near zero on the other side [21], [22]. The configuration where the magnets are arranged around a circle in an alternating pattern is particularly appealing for our application due to the presence of a central window that can be used for imaging.

Fig. 1 illustrates the proposed steering paradigm. The magnetic field is uniform along the central axis of the multipole ring magnet, including the actuation plane; therefore, the instrument will predominantly experience magnetic torque. Rotation of the ring magnet realigns the field lines for in-plane steering, while the head of the instrument bends outside the plane upon translation of the ring magnet (see Video 1). Section II describes the design of the magnet configuration, Section III introduces the experimental platform, and Section IV demonstrates that a new class of endovascular instruments, flow-driven microcatheters [12], [23], [24], can be navigated inside perfused biomimetic vessel phantoms using our experimental platform.

Manuscript received: August, 12, 2025; Revised November, 6, 2025; Accepted December, 5, 2025.

This paper was recommended for publication by Jessica Burgner-Kahrs upon evaluation of the Associate Editor and Reviewers' comments.

Authors are with the Institute of Mechanical Engineering, Ecole Polytechnique Fédérale de Lausanne (EPFL), CH-1015 Lausanne, Switzerland (e-mail: julian.raub@epfl.ch; pancaldi.lucio@gmail.com; loic.vondeschwanden@epfl.ch; selman.sakar@epfl.ch).

Corresponding author: Mahmut Selman Sakar

Digital Object Identifier (DOI): see top of this page.

IEEE Robotics and Automation Letters (RA-L) paper, presented at ICRA 2026, Vienna, Austria. Cite as RA-L paper.

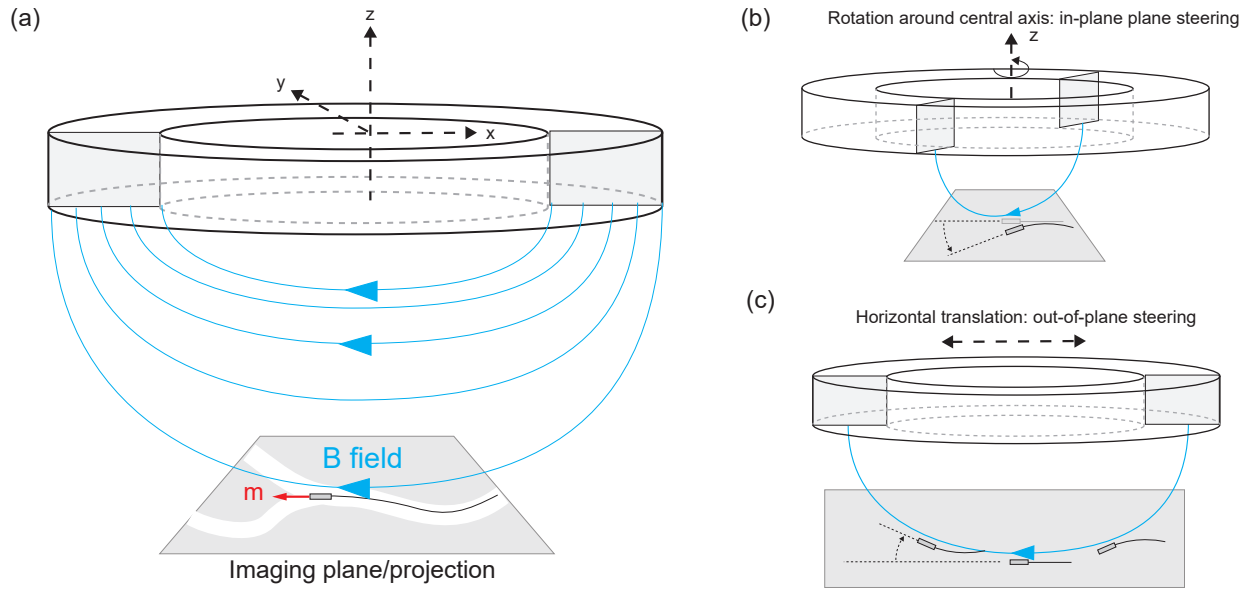

Fig. 1. Schematic representation of the steering principle. The multipole ring magnet generates a purely horizontal magnetic field along the central axis of the ring including the imaging plane where the magnetic head of the endovascular instrument is located. Rotating the ring magnet around z axis reorients the magnetic head in the xy plane, which is referred as in-plane steering. Translating the ring magnet along the x axis bends the head in the xz plane, which is referred as out-of-plane steering.

II. Design of the Magnet Configuration

The design of the magnetic navigation system builds upon the concept of Halbach arrays, which are known for producing a strong and uniform magnetic field within a closed ring of magnets. In Halbach's original formulation [22], an idealized array of infinitely long line dipoles satisfies the relationship $\tan(\beta_i) = 2\tan(\gamma_i)$, where γ_i defines the angular position of the ith magnet on the ring and β_i its magnetization orientation relative to the x-axis. This configuration maximizes the internal field strength and uniformity while having little stray fields outside. However, when magnets have finite dimensions, this analytical relationship no longer guarantees maximal field strength at the center of the ring, as has been shown in recent work [25], [26]. In addition, the uniform field predicted by the ideal Halbach model is only optimal within the magnets' plane, whereas our navigation system requires a controllable field at a distance above or below the ring.

To meet these practical requirements, our design must therefore (i) generate maximal magnetic field strength at the actuation point that is located along the central axis of the ring, (ii) preserve a central aperture for unobstructed fluoroscopic imaging, (iii) produce a dominant horizontal field along the central axis of the ring, and (iv) maintain symmetry and uniformity for stable control. The last point led us to consider that a symmetric arrangement similar to a Halbach array would be most suited for our case.

Fig. 2 illustrates the spatial arrangement of four identical permanent magnets, labeled $\vec{m}_1$, $\vec{m}_2$, $\vec{m}_3$, $\vec{m}_4$, positioned symmetrically around a central axis. Each magnet is characterized by its magnetization vector $\vec{m}_i$ and three orientation parameters α_i, β_i, and γ_i. The angle α_i denotes the pitch of the magnet with respect to the y-axis, β_i represents the yaw angle around the z-axis, and γ_i determines the angular position of the magnet's center along the ring of radius R in the x–y plane.

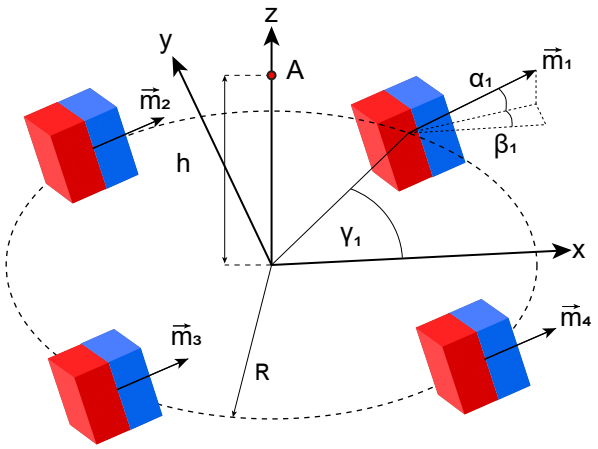

Fig. 2. Illustration of the 4-magnet configuration showing the magnetization vectors $\vec{m}_1$, $\vec{m}_2$, $\vec{m}_3$, $\vec{m}_4$ and the orientation parameters α_1, β_1, γ_1.

Let us consider a point A at a distance h from the origin along the z axis where we would like to calculate the magnetic field. For this configuration, the four magnets are located at

IEEE Robotics and Automation Letters (RA-L) paper, presented at ICRA 2026, Vienna, Austria. Cite as RA-L paper.

the following positions with respect to point A:

$$\vec{\mathbf{r}}_1 = \begin{bmatrix} -R\cos(\gamma_1) \\ -R\sin(\gamma_1) \\ h \end{bmatrix}, \quad \vec{\mathbf{r}}_2 = \begin{bmatrix} -R\cos(\gamma_2) \\ -R\sin(\gamma_2) \\ h \end{bmatrix},$$
$$\vec{\mathbf{r}}_3 = \begin{bmatrix} -R\cos(\gamma_3) \\ -R\sin(\gamma_3) \\ h \end{bmatrix}, \quad \vec{\mathbf{r}}_4 = \begin{bmatrix} -R\cos(\gamma_4) \\ -R\sin(\gamma_4) \\ h \end{bmatrix}. \tag{1}$$

$$||\vec{r}_1|| = ||\vec{r}_2|| = ||\vec{r}_3|| = ||\vec{r}_4|| = r \tag{2}$$

Each dipole moment $\mathbf{m}_i$ is parameterized using the pitch and yaw angles as follows:

$$\vec{\mathbf{m}}_i = m \begin{bmatrix} \cos\alpha_i \cos\beta_i \\ \cos\alpha_i \sin\beta_i \\ \sin\alpha_i \end{bmatrix}, \tag{3}$$

where m is the magnitude of the dipole moment of the magnets. The total magnetic field at test point A is the vector sum of the contributions from all four magnets:

$$\vec{\mathbf{B}}_{\text{total}} = \sum_{i=1}^{4} \vec{B}_i. \tag{4}$$

Substituting the dipole field equation for each magnet, the total field can be written as:

$$\vec{B}_{\text{total}} = \frac{\mu_0}{4\pi r^3} \sum_{i=1}^{4} \left[\frac{3(\vec{m}_i \cdot \vec{r}_i)\vec{r}_i}{r^2} - \vec{m}_i \right]. \tag{5}$$

The Cartesian components of $\vec{B}_{\text{total}}$ are:

$$B_x = \frac{\mu_0}{4\pi r^3} \left[\frac{3x}{r^2}(-a+b+c-d) - m\sum_{i=1}^{4} \cos(\alpha_i)\cos(\beta_i) \right] \tag{6}$$

$$B_y = \frac{\mu_0}{4\pi r^3} \left[\frac{3y}{r^2}(-a-b+c+d) - m\sum_{i=1}^{4} \cos(\alpha_i)\sin(\beta_i) \right] \tag{7}$$

$$B_z = \frac{\mu_0}{4\pi r^3} \left[\frac{3h}{r^2}(a+b+c+d) - m\sum_{i=1}^{4} \sin(\alpha_i) \right] \tag{8}$$

where a, b, c, and d are $m_{ix}r_{ix} + m_{iy}r_{iy} + m_{iz}r_{iz}$ for $i = 1, 2, 3, 4$, respectively, and $x = |R\cos(\gamma_i)|$ and $y = |R\sin(\gamma_i)|$.

To determine the maximum total magnetic field along the x-axis, we first identify the orientation of each individual magnet that maximizes its B_x contribution. By evaluating the maximum B_x field produced by each magnet, the overall maximum attainable field can be estimated as the sum of these individual maxima. This approach is justified by the generalized triangle inequality,

$$\max\left(\sum_i B_{x,i}\right) \leq \sum_i \max(B_{x,i}), \tag{9}$$

which ensures that the global maximum of the total field cannot exceed the sum of the individual maxima.

The specific orientation that maximizes B_x for each magnet can be found by taking the partial derivatives of B_x with respect to α_i and β_i as zero.

The derivative of B_x with respect to α_i is:

$$\begin{aligned} \frac{dB_x(\vec{r}_i, \vec{m}_i)}{d\alpha_i} =& \frac{\mu_0 m}{4\pi r^3} \Bigg[\frac{3r_{ix}}{r^2} \Big(-r_{ix}\sin(\alpha_i)\cos(\beta_i) \\ & - r_{iy}\sin(\alpha_i)\sin(\beta_i) + r_{iz}\cos(\alpha_i) \Big) \\ & + \sin(\alpha_i)\cos(\beta_i) \Bigg] = 0. \end{aligned} \tag{10}$$

Solving for α_i gives:

$$\alpha_i = \tan^{-1}\left(\frac{r_{ix}r_{iz}}{r_{ix}^2\cos(\beta_i) + r_{ix}r_{iy}\sin(\beta_i) - \frac{r^2}{3}\cos(\beta_i)} \right). \tag{11}$$

The derivative of B_x with respect to β_i is:

$$\begin{aligned} \frac{dB_x(\vec{r}_i, \vec{m}_i)}{d\beta_i} =& \frac{\mu_0 m}{4\pi r^3} \Bigg[\frac{3r_{ix}}{r^2} \Big(-r_{ix}\cos(\alpha_i)\sin(\beta_i) \\ & + r_{iy}\cos(\alpha_i)\cos(\beta_i) \Big) \\ & + \cos(\alpha_i)\sin(\beta_i) \Bigg] = 0. \end{aligned} \tag{12}$$

Solving for β_i gives:

$$\beta_i = \tan^{-1}\left(\frac{-r_{ix}r_{iy}}{-r_{ix}^2 + \frac{r^2}{3}} \right). \tag{13}$$

Substituting r_{ix} r_{iy}, and r_{iz} with their respective components from Equation 1 reveals that the maximum field strength is achieved when the following conditions are met:

$$\alpha_1 = -\alpha_2 = -\alpha_3 = \alpha_4, \quad \beta_1 = -\beta_2 = \beta_3 = -\beta_4. \tag{14}$$

B_y and B_z components are derived by substituting the optimized orientation angles α_{1-4} and β_{1-4} into Equations (7) and (8). The values of these components are found to be zero, thereby confirming that the magnetic field is exclusively directed along the x-axis. This cancellation of the y and z components arises naturally from the imposed mirror symmetry of the magnet arrangement with respect to both x and y axes.

IEEE Robotics and Automation Letters (RA-L) paper, presented at ICRA 2026, Vienna, Austria. Cite as RA-L paper.

A. 8-magnet Configuration and Central Imaging Window

Going from four to the eight-magnet configuration is motivated by the desire to populate the available positions along the circumference of the ring magnet. We postulated that by filling the available space with additional magnets, we could enhance magnetic field strength and uniformity while preserving imaging compatibility. During out-of-plane steering, translation of the ring along the x-axis can obstruct the catheter in the fluoroscopic image if the magnets are arranged close to the x axis. To address this limitation, we introduce a *side window* of width w, to open up a path for out-of-plane steering, which ensures continuous and unobstructed visualization of the catheter by preventing the magnet from blocking the view.

We built a prototype that consists of eight 2x2x2 cm^3 cubic NdFeB magnets of remanence $B_r = 1.4$ T that are encased in a 3D printed cage. We set the aperture radius R as 4.5 cm considering the trade-off between magnetic field concentration and spatial clearance as well as the need for a sufficiently large opening for microcatheter visualization. Next, we computed the magnetic field strength at a distance of $z = 10\,\text{cm}$ as a function of γ_1 and γ_2. Calculations showed that smaller γ values result in stronger magnetic field (see Fig.3). However, practical constraints imposed by the system's mechanical design and imaging requirements dictate the final configuration. Specifically, γ_1 was set to 25° to provide a side window w of 1.8 cm for fluoroscopic visualization of the magnetic instrument during out-of-plane steering. Although minimizing γ_2 would maximize field strength, there is a strong repulsive force between adjacent magnets. The lowest feasible angle that allowed physical assembly was $\gamma_2 = 70°$.

Once γ_1 and γ_2 are defined, the remaining magnet positions are directly obtained by enforcing mirror symmetries with respect to the x- and y-axes. All tilt angles β_i are set to zero to preserve a sufficiently large side window w, which is essential for unobstructed imaging during out of plane steering. This design compromise is justified, as the resulting decrease in magnetic field strength at 10 cm is below 0.1 mT, a negligible loss compared to the geometric advantage. The angles chosen for the final prototype are shown in Table I.

TABLE I
VALUES OF ANGULAR PARAMETERS FOR THE BUILT PROTOTYPE

Parameter	α (deg)	β (deg)	γ (deg)
Magnet 1	245	0	25
Magnet 2	−245		155
Magnet 3	−245		205
Magnet 4	245		335
Magnet 5	204		70
Magnet 6	−204		110
Magnet 7	−204		250
Magnet 8	204		290

III. MAGNETIC FIELD CHARACTERISATION

We computed the magnetic field produced by the multipole ring magnet to investigate the spatial distribution of the field in the xz plane (Fig. 4). At $z = -5\,\text{cm}$, the field magnitude inside the visible workspace is close to 20 mT, increasing slightly to 25 mT near the edges of the aperture. At $z = -10\,\text{cm}$, the field magnitude is close to 5 mT.

We performed magnetic field measurements to validate the predictions of the theoretical model. A three-axis Hall sensor (TLE493D) was mounted on an XY stage constructed from two orthogonal linear stages (VT-80, PI). The sensor was

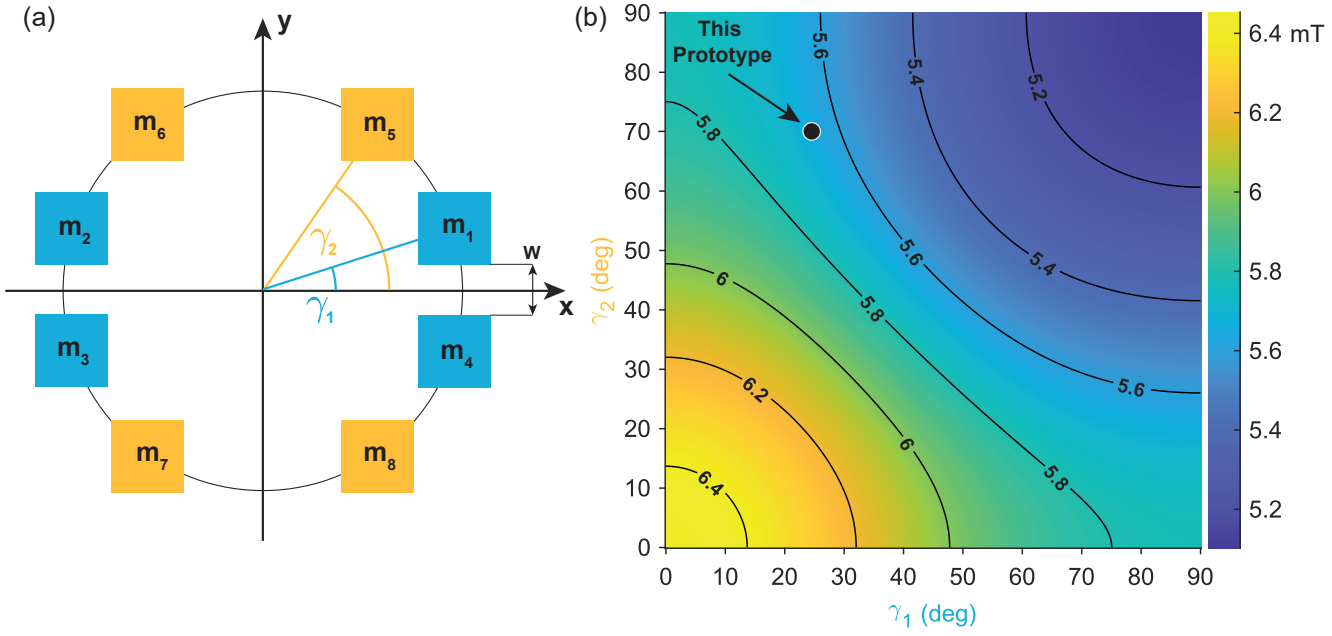

Fig. 3. Design optimization for magnet placement. (a) Schematic view of the ring magnet geometry, highlighting the field-of-view window w that enables visualization of the microcatheter during out-of-plane steering. The choice of γ_1 is determined by imaging requirements while γ_2 is constrained by manufacturing issues due to magnet–magnet interactions. (b) Simulated magnetic field magnitude at a distance of $z = 10\,\text{cm}$ for varying angular parameters γ_1 and γ_2. Lower γ angles yield stronger magnetic fields. The marker indicates the selected design values: $\gamma_1 = 25°$, $\gamma_2 = 70°$.

IEEE Robotics and Automation Letters (RA-L) paper, presented at ICRA 2026, Vienna, Austria. Cite as RA-L paper.

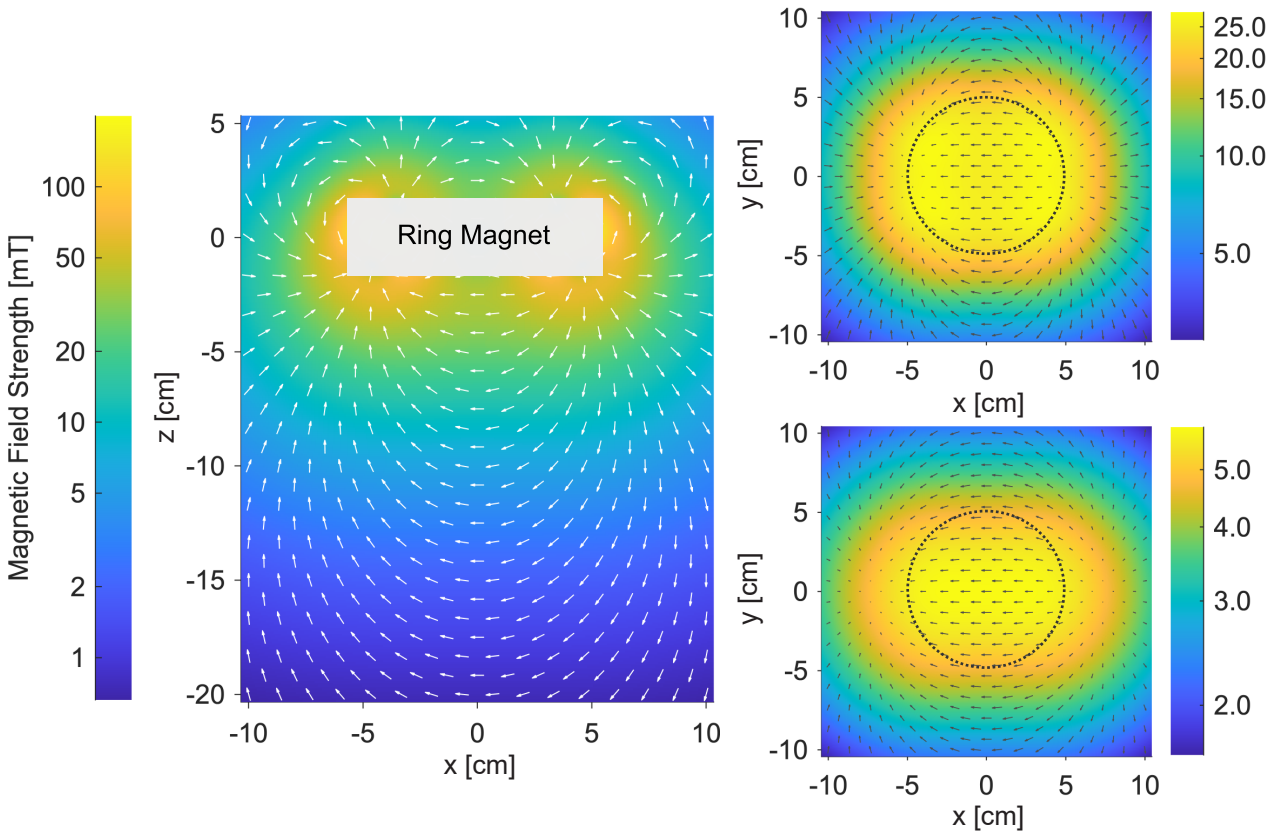

Fig. 4. Magnetic field distribution below the multipole ring magnet. The images show the field distribution on the xz plane (left) and xy plane at z = -5 cm (top right) and z = -10 cm (bottom right). The arrows show the normalized direction of the magnetic field lines, and the colors denote the magnitude. The overlaid black circle denotes the visible workspace with the center of each of the 8 magnets positioned along the circumference of the circle

translated inside a 10×10 cm plane at 1 cm resolution. This mapping was repeated for z distances ranging from 5 cm to 10 cm in 1 cm increments. At each measurement point, the magnetic field vector was recorded and compared with the theoretical results. We computed the average angular deviation between the measured and computed field vectors as well as the relative error in field magnitude. The results showed strong agreement with a mean angular error of 2° and a magnitude error of less than 2%, thereby confirming the validity of using the point dipole approximation to calculate the magnetic field generated by our system.

IV. Microcatheter Navigation

We assembled a magnetic navigation system (see Fig.5) by mounting the multipole ring magnet on a ring gear actuated by a linear stepper motor (NEMA17). The rotation of the motor is controlled using a custom-made joystick, which communicates with a stepper motor driver (TMCM-1070, Trinamic) through a microcontroller (Arduino Uno). This end-effector is mounted on a metal post (Thorlabs) that is translated by a linear stage (VT-80, PI) via its motion controller (C-884.4DC, PI).

We used a 1.8 m long flow-driven magnetic microcatheter with a 1.5 mm long, 250 μm diameter magnetic head. We refer the reader to a recent publication [12] for the details of manufacturing and operation of flow-driven microcatheters. Briefly, the microcatheter consists of a magnetic head made of PDMS and NdFeB powder, a microfabricated polyimide ribbon that inflates upon being pressurized, and a reinforced cylindrical tube. Vascular phantoms were 3D printed (Formlabs 3B+) from a transparent resin (BioMed Clear) to demonstrate 3D magnetic steering. The phantoms were connected to a closed loop flow system and perfused with deionized water using a peristaltic pump (LP-BT100-2J, Drifton) at a constant physiological flow rate of 64 mL/min.

A. In-Plane Steering

Fig. 6a shows an overview of the vascular phantom. The main vessel has a diameter of 2.5 mm and bifurcates into two side branches with diameters of 1.5 mm. The branching angles are 45° and 90° relative to the main axis, respectively. The flow-driven magnetic microcatheter was manually inserted from the inlet, and the ring magnet was rotated about its central axis to orient the magnetic field on the imaging plan according to the vessel geometry. The rotation of the ring magnet induces a torque on the magnetic head, resulting in gradual tip deflection.

Fig. 6b displays time-lapse images acquired during a navigation trial (see Video 1). The system was manually controlled using a joystick. The catheter tip bent according to the magnetic field orientation, enabling redirection of the catheter toward different vessel branches. The average time to reach the first bifurcation from the phantom entry point was 6.5 ± 1.43 s

IEEE Robotics and Automation Letters (RA-L) paper, presented at ICRA 2026, Vienna, Austria. Cite as RA-L paper.

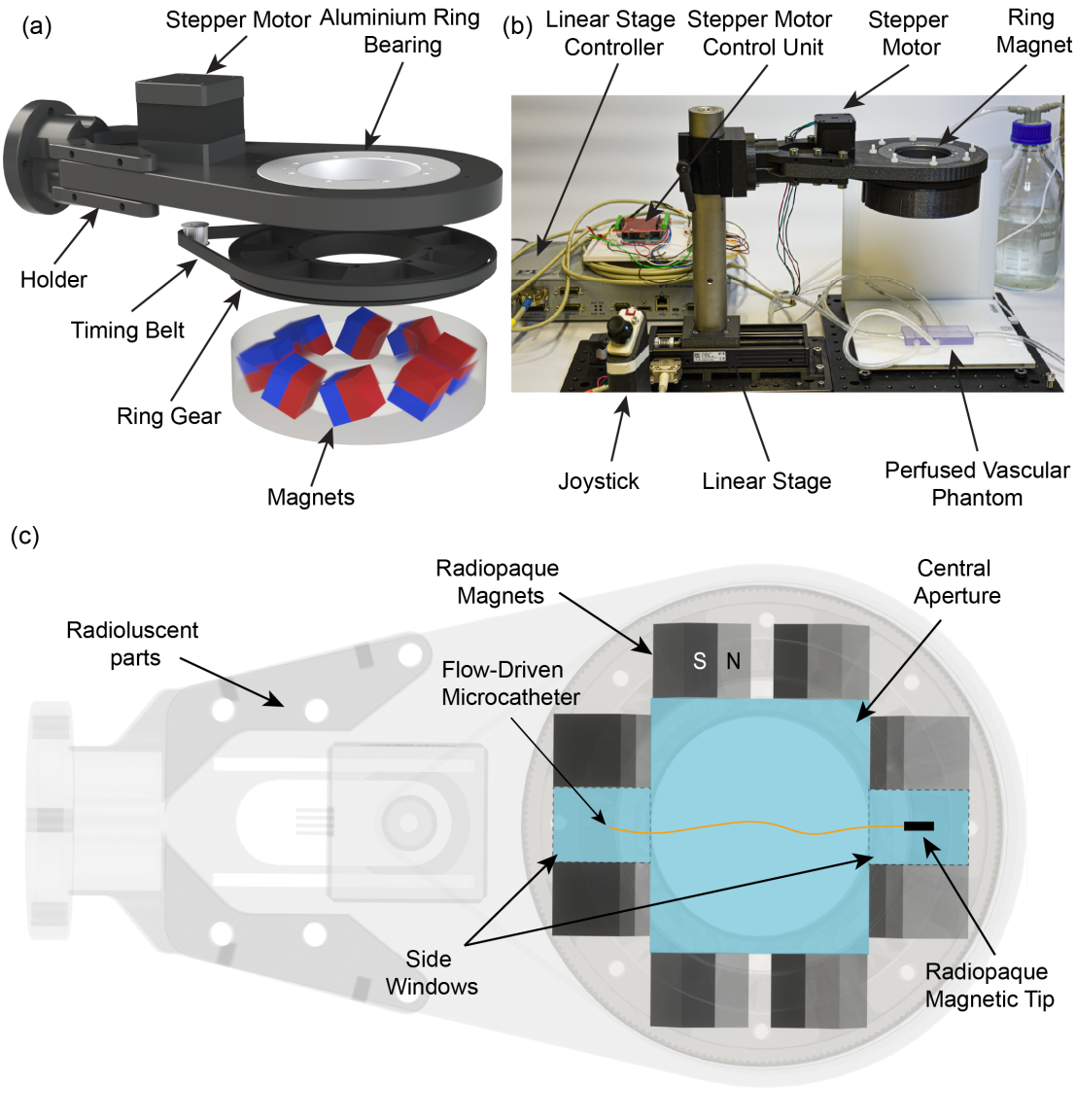

Fig. 5. Experimental platform for magnetic catheter navigation. (a) Annotated rendering of the ring magnet assembly, showing key mechanical components including the ring gear, timing belt, holder, stepper motor, and aluminum bearing structure. (b) Photograph of the full experimental setup, including the joystick-controlled stepper motor, linear stage with controller, and the perfused vascular phantom positioned beneath the magnet for in vitro testing.(c) Rendering of the top view of the magnetic actuation system as would be visualized under fluoroscopy. The 3D-printed components and motor are radiolucent, allowing X-rays to pass through and reveal underlying anatomical features. In contrast, the permanent magnets are radiopaque, obstructing the view of structures located behind them. The system includes a central aperture that provides a direct line of sight for imaging, as well as two side windows that enable visualization of the radiopaque magnetic tip of the flow-driven microcatheter during out-of-plane steering.

(n = 10) and navigating from the entry point to the second bifurcation took 14.8 ± 1.90 s (n = 10).

B. Out-of-Plane Steering

Fig. 6c shows a side view of the platform with superimposed magnetic field vectors illustrating the field distribution in the xz plane. Translating the ring magnet along the x axis while maintaining a fixed angular orientation changes the direction of the magnetic field vector relative to the imaging plane, resulting in a vertical torque component that bends the magnetic tip of the catheter out of the plane (Fig. 6d). We used a vessel phantom that contains an upward-curved vessel segment that bifurcates into two branches to demonstrate 3D endovascular navigation.

A magnified view of the phantom shows the position of the magnetic tip within the vascular structure (Fig. 6e). Fig. 6f shows a time-lapse sequence of the catheter tip undergoing out-of-plane deflection (see Video 1). As the ring magnet was translated back, the tip gradually bent upwards into the upper bifurcation. Advancement in the upper left bifurcation was achieved by rotating the ring magnet counterclockwise. The average time to complete the entire path from the point 1 to point 4 took 40.5 ± 14.5 s (n = 10).

IEEE Robotics and Automation Letters (RA-L) paper, presented at ICRA 2026, Vienna, Austria. Cite as RA-L paper.

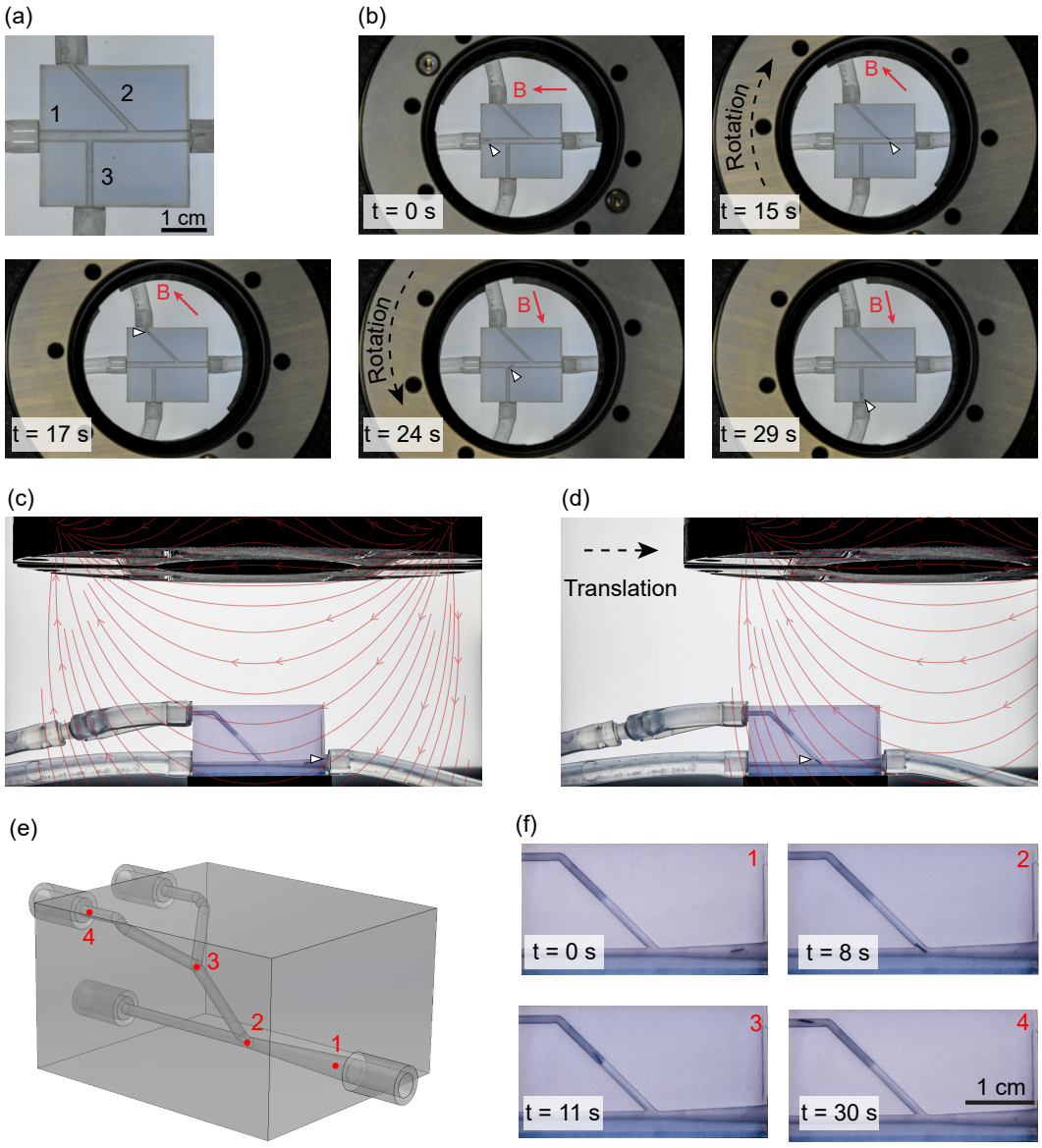

Fig. 6. In-plane steering of a flow-driven magnetic microcatheter in a planar vascular phantom. (a) Overview of the phantom geometry consisting of a 2.5 mm diameter main vessel and two side branches with diameters of 1.5 mm branching at 45° and 90°. (b) Time-lapse sequence showing the gradual lateral deflection of the catheter tip in response to rotation of the ring magnet at $t = 0$, 15, 17, 24, and 29 s. Red arrows indicate the direction of the applied magnetic field at each time point and the white arrows indicate the position of the magnetic tip of the microcatheter. (c) Side view of the platform showing the phantom used for 3D navigation. The red overlaid arrows show the magnetic field distribution underneath the ring magnet and the white arrow shows the position of the magnetic tip of the flow driven microcatheter. (d) Side view of the platform after translating the ring magnet to the right by 30 mm with respect to the phantom. This translation leads to an upward magnetic field at the catheter location leading to out of plane bending of the magnetic tip. (e) 3D view of the phantom used in panel (c) (d) and (f) highlighting the navigation waypoints in red. (f) Time-lapse images during the navigation of the microcatheters. Pictures correspond to the waypoints shown in panel (e).

V. Discussion

The proposed multipole ring magnet is a compact and versatile tool for steering magnetic endovascular instruments. The eight-magnet configuration was derived from theoretical considerations to achieve uniform magnetic field within a central workspace while maximizing field strength. The same conditions that yield a purely horizontal field also maximize the dominant field component, simplifying the design and optimization process. The current implementation achieves a magnetic field of 20 mT in the center of the workspace at a distance of 5 cm from the magnet face, which is sufficient to actuate a flow-driven microcatheter with a magnetic tip. However, the field strength drops to approximately 5 mT at 10 cm, limiting the effective working depth. Applications requiring deeper actuation or stronger torque would benefit from higher grade and/or larger magnets. Increasing the size of the magnets from 2 cm to 4 cm and adjusting the radius of the ring magnet accordingly would increase the field strength to 36 mT at a distance of 10 cm.

In the current design, all yaw angles (β_i) were set to zero.

IEEE Robotics and Automation Letters (RA-L) paper, presented at ICRA 2026, Vienna, Austria. Cite as RA-L paper.

This simplification ensures a sufficiently large side window and only decreases the maximum magnetic field strength by less than 0.1 mT at a distance of 10 cm. Nevertheless, this decision may constrain the achievable field configurations. Future iterations will consider nonzero yaw angles to enable more flexible and asymmetric field shaping.

While the focus was on generating uniform fields to apply torque, the resulting field distributions inevitably include gradient components that produce magnetic forces. In this study, magnetic field gradients were not explicitly optimized or measured. These forces were not observed to affect the navigation of flow-driven microcatheter in experiments with vessel phantoms but they may play a role in other applications, particularly those involving untethered or force-sensitive magnetic agents. To mitigate undesired magnetic forces, future implementations may require the incorporation of a second ring magnet positioned symmetrically on the opposite side of the navigation plane. Such a configuration would enable force cancellation through superposition, effectively neutralizing gradient-induced forces while preserving torque generation.

Although the design is intended to be imaging-compatible by providing a central aperture, fluoroscopic compatibility was not quantitatively evaluated. Future studies should characterize potential image artifacts introduced by the ring magnet during operation, particularly under clinical imaging conditions. Mounting the system directly onto the fluoroscope arm represents a promising approach that would synchronize the motion of the fluoroscope and the ring magnet. This integration inherently resolves the issue of image-to-magnet registration, thereby simplifying the requirements for automation and closed-loop control. We envision that this system could serve as a simple and low-cost alternative to commercially available clinical magnetic navigation systems.

ACKNOWLEDGMENT

The authors acknowledge technical support by the Center of MicroNanoTechnology (CMi) team at EPFL during the fabrication of the flow-driven microcatheters. We thank Mehdi Gadiri for his contributions to the design and manufacturing of the flow-driven microcatheters and Lorenzo Noseda for fruitful discussions. L.P. acknowledges funding from BRIDGE Proof of Concept (40B1-0_209182) and Innogrant (S133-IN-23-06).

REFERENCES

[1] H. Tillander, "Magnetic guidance of a catheter with articulated steel tip," *Acta radiologica*, vol. 35, no. 1, pp. 62–64, 1951.

[2] J. Driller, S. Hilal, W. Michelsen, B. Sollish, B. Katz, and W. Konig Jr, "Development and use of the pod catheter in the cerebral vascular system," *Medical research engineering*, vol. 8, no. 4, pp. 11–16, 1969.

[3] J. Driller, "Kinetics of magnetically guided catheters," *IEEE Transactions on Magnetics*, vol. 6, no. 3, pp. 467–471, 1970.

[4] D. Montgomery, J. Hale, N. Pierce, and S. Yodh, "A magnetically guided catheter system for intercranial use in man," *IEEE Transactions on Magnetics*, vol. 6, no. 2, pp. 374–374, 1970.

[5] J. Molcho, H. Karny, E. H. Frei, and H. M. Askenasy, "Selective cerebral catheterization," *IEEE Transactions on Biomedical Engineering*, no. 2, pp. 134–140, 1970.

[6] A. Azizi, C. C. Tremblay, K. Gagné, and S. Martel, "Using the fringe field of a clinical mri scanner enables robotic navigation of tethered instruments in deeper vascular regions," *Science Robotics*, vol. 4, no. 36, p. eaax7342, 2019.

[7] Y. Kim, E. Genevriere, P. Harker, J. Choe, M. Balicki, R. W. Regenhardt, J. E. Vranic, A. A. Dmytriw, A. B. Patel, and X. Zhao, "Telerobotic neurovascular interventions with magnetic manipulation," *Science Robotics*, vol. 7, no. 65, p. eabg9907, 2022.

[8] J. Hwang, S. Jeon, B. Kim, J.-y. Kim, C. Jin, A. Yeon, B.-J. Yi, C.-H. Yoon, H.-J. Park, S. Pané *et al.*, "An electromagnetically controllable microrobotic interventional system for targeted, real-time cardiovascular intervention," *Advanced healthcare materials*, vol. 11, no. 11, p. 2102529, 2022.

[9] M. E. Tiryaki, Y. G. Elmacıoğlu, and M. Sitti, "Magnetic guidewire steering at ultrahigh magnetic fields," *Science Advances*, vol. 9, no. 17, p. eadg6438, 2023.

[10] R. Dreyfus, Q. Boehler, S. Lyttle, P. Gruber, J. Lussi, C. Chautems, S. Gervasoni, J. Berberat, D. Seibold, N. Ochsenbein-Kölble *et al.*, "Dexterous helical magnetic robot for improved endovascular access," *Science Robotics*, vol. 9, no. 87, p. eadh0298, 2024.

[11] M. Zhang, L. Yang, H. Yang, L. Su, J. Xue, Q. Wang, B. Hao, Y. Jiang, K. F. Chan, J. J. Y. Sung *et al.*, "A magnetically actuated microcatheter with soft rotatable tip for enhanced endovascular access and treatment efficiency," *Science advances*, vol. 11, no. 25, p. eadv1682, 2025.

[12] L. Pancaldi, E. Özelçi, M. A. Gadiri, J. Raub, P. J. Mosimann, and M. S. Sakar, "Flow-driven magnetic microcatheter for superselective arterial embolization," *Science Robotics*, vol. 10, no. 107, p. eadu4003, 2025.

[13] B. J. Nelson, B. R. Bendok, E. L. Turcotte, and H. H. Batjer, "Remote magnetic navigation enables precision telesurgery," *Science Robotics*, vol. 9, no. 87, p. eado3187, 2024.

[14] J. Hwang, J.-Y. Kim, and H. Choi, "A review of magnetic actuation systems and magnetically actuated guidewire-and catheter-based microrobots for vascular interventions," *Intelligent Service Robotics*, vol. 13, no. 1, pp. 1–14, 2020.

[15] M. N. Faddis, W. Blume, J. Finney, A. Hall, J. Rauch, J. Sell, K. T. Bae, M. Talcott, and B. Lindsay, "Novel, magnetically guided catheter for endocardial mapping and radiofrequency catheter ablation," *Circulation*, vol. 106, no. 23, pp. 2980–2985, 2002.

[16] S. Gervasoni, N. Pedrini, T. Rifai, C. Fischer, F. C. Landers, M. Mattmann, R. Dreyfus, S. Viviani, A. Veciana, E. Masina *et al.*, "A human-scale clinically ready electromagnetic navigation system for magnetically responsive biomaterials and medical devices," *Advanced Materials*, vol. 36, no. 31, p. 2310701, 2024.

[17] M. P. Armacost, J. Adair, T. Munger, R. R. Viswanathan, F. M. Creighton, D. T. Curd, and R. Sehra, "Accurate and reproducible target navigation with the stereotaxis niobe® magnetic navigation system," *Journal of Cardiovascular Electrophysiology*, vol. 18, pp. S26–S31, 2007.

[18] G. Pittiglio, M. Brockdorff, T. da Veiga, J. Davy, J. H. Chandler, and P. Valdastri, "Collaborative magnetic manipulation via two robotically actuated permanent magnets," *IEEE Transactions on Robotics*, vol. 39, no. 2, pp. 1407–1418, 2022.

[19] S. E. Wright, A. W. Mahoney, K. M. Popek, and J. J. Abbott, "The spherical-actuator-magnet manipulator: A permanent-magnet robotic end-effector," *IEEE Transactions on Robotics*, vol. 33, no. 5, pp. 1013–1024, 2017.

[20] P. Ryan and E. Diller, "Magnetic actuation for full dexterity microrobotic control using rotating permanent magnets," *IEEE Transactions on Robotics*, vol. 33, no. 6, pp. 1398–1409, 2017.

[21] J. Mallinson, "One-sided fluxes–a magnetic curiosity?" *IEEE Transactions on magnetics*, vol. 9, no. 4, pp. 678–682, 1973.

[22] K. Halbach, "Design of permanent multipole magnets with oriented rare earth cobalt material," *Nuclear instruments and methods*, vol. 169, no. 1, pp. 1–10, 1980.

[23] L. Pancaldi, P. Dirix, A. Fanelli, A. M. Lima, N. Stergiopulos, P. J. Mosimann, D. Ghezzi, and M. S. Sakar, "Flow driven robotic navigation of microengineered endovascular probes," *Nature communications*, vol. 11, no. 1, p. 6356, 2020.

[24] L. Pancaldi, L. Noseda, A. Dolev, A. Fanelli, D. Ghezzi, A. J. Petruska, and M. S. Sakar, "Locomotion of sensor-integrated soft robotic devices inside sub-millimeter arteries with impaired flow conditions," *Advanced Intelligent Systems*, vol. 4, no. 5, p. 2100247, 2022.

[25] I. Rehberg and P. Blümler, "Analytic approach to creating homogeneous fields with finite-size magnets," *Physical Review Applied*, vol. 23, no. 6, p. 064029, 2025.

[26] S. Tewari, T. O'Reilly, and A. Webb, "Improving the field homogeneity of fixed-and variable-diameter discrete halbach magnet arrays for mri via optimization of the angular magnetization distribution," *Journal of Magnetic Resonance*, vol. 324, p. 106923, 2021.